Depolarization and blurring of optical images by biological tissues

Miguel Moscoso, Joseph B. Keller, and George Papanicolaou

Department of Mathematics, Stanford University, Stanford CA 94305, USA

mmoscoso@math.stanford.edu, jbk@math.stanford.edu, papanico@math.stanford.edu

We present a study of the image blurring and depolarization resulting from the transmission of a narrow beam of light through a continuous random medium. We investigate the dependence of image quality degradation and of the depolarization on optical thickness, correlation length of the inhomogeneities, and incident polarization state. This is done numerically with a Monte Carlo method based on a transport equation which takes into account polarization of light. We compare our results with transport in media with discrete spherical scatterers. We show that depolarization effects are different in the two models.

OCIS codes: 170.3660,170.7050,260.5430,030.5620

1. Introduction

Optical imaging through scattering media has been intensively investigated over the last few years in different fields, such as atmospheric remote sensing,[1–3] underwater photography,[4] biological optics,[5–7] and medical imaging.[8–11] Because multiple scattering results in image blurring, various techniques (e.g., time gating, optical coherence, confocal detection, etc ...) have been devised to overcome this difficulty. All these techniques discriminate between weakly and strongly scattered photons. More recently, methods involving polarization effects have attracted significant interest for their simplicity and low cost.[12–14] Multiple scattering gives rise to diffusion of the total intensity, and also to depolarization. Schmitt *et al.*[12] showed experimentally that a polarization-sensitive technique could discriminate between short path photons (carrying the information) and long path photons transmitted through opti-

cally thick media. Their results clearly displayed that polarization-sensitive methods gave better contrast of images of absorbing strips in highly scattering media. Depolarization effects can be used as a discrimination criterion because the polarization of short-path photons (ballistic and snake photons) differs from that of long-path photons (diffusive photons).

We shall consider transmission of narrow polarized laser beams through biological tissues. Usually, a biological tissue is modeled as a medium containing discrete spherical particles of the same or different sizes. However, it is not likely that spherical inclusions are adequate to represent tissue inhomogeneities. On a microscopic scale, tissue does not have clear boundaries between its different constituents. Instead, random low contrast inhomogeneities (of the order of 5 %) in the refractive index are observed in most soft tissues.[15] This suggests an approach based on the theory of wave propagation in continuous random media, where light scattering is not due to the discontinuities in refractive index. Moreover, Sankaran *et al.*[7] have reported recently on the distinctly different polarization effects in common tissue phantoms composed of microspheres diluted in water[16–18] and biological tissues.

The theory of radiative transfer, employing Stokes parameters, can be used to describe light propagation through a medium. Analytical solutions are not known except in simple particular cases, such as plane parallel atmospheres with a constant net flux.[19] When the incident laser beam is narrow no solution is known. Therefore we have developed a Monte Carlo method to obtain the spatial distribution of the total intensity and of the polarization components of the transmitted beam. The magnitudes of these components and of the total intensity for a narrow incident beam are called the point-spread functions. The analysis of the degradation of the image and of the depolarization is usually done in terms of these functions.[20–22]

In the next section we describe our model and we discuss how it differs from models that consider media with discrete spherical scatterers. In the third section we describe a Monte Carlo method for three-dimensional problems. It solves the radiative transport equation, as is explained in Appendix A, and it is exact up to statistical errors. Section four contains the numerical results for the point-spread functions. It also presents the results of a numerical experiment which demonstrates that polarization-sensitive techniques can improve the image quality of a target embbeded in turbid media. The last section contains our conclusions.

2. Scattering process for the Stokes parameters

A. Weakly fluctuating random media versus microsphere suspensions

Biological tissues is a medium varying randomly in space containing inhomogeneities with no clear boundaries. We describe it as a medium with weak random fluctuations of the dielectric permittivity $\epsilon(\mathbf{r}) = \epsilon_0[1 + \delta\epsilon(\mathbf{r})]$, where $\mathbf{r}$ denotes position and $\delta\epsilon(\mathbf{r})$ is the random fractional permittivity fluctuation. We suppose that it is illuminated

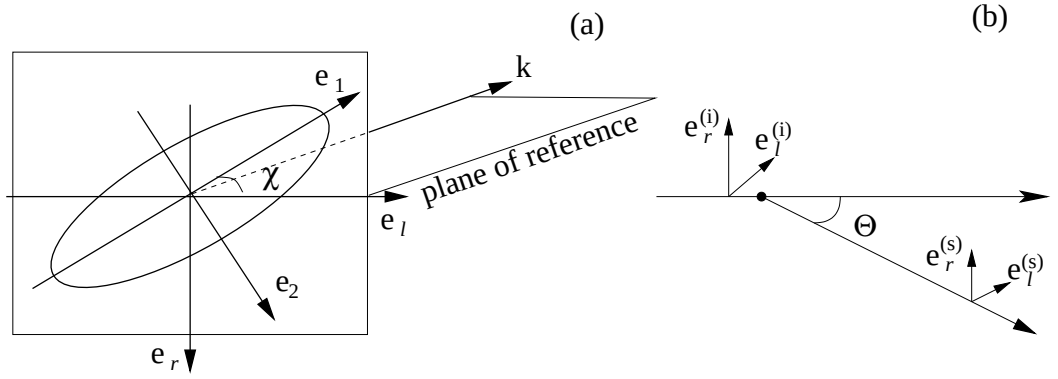

Fig. 1. (a) Polarization ellipse for a transverse wave. (b) Coordinate system for the polarization parameters of the incident and scattered waves in single scattering. The scattering plane is defined by the incident and scattered directions, and l and r stand for directions parallel and perpendicular to the plane of reference, respectively, in planes transverse to the incident and scattered waves.

by a light source. Due to interaction with the inhomogeneities, light waves with wave vector $\mathbf{k}'$ at point $\mathbf{r}$ can scatter into any direction $\hat{\mathbf{k}}$ with wave vector $\mathbf{k}$, where $\hat{\mathbf{k}} = \mathbf{k}/|\mathbf{k}|$. The statistical properties of the light propagating through the medium can be specified by the Stokes vector (see Appendix A)

$$\mathbf{I} = \begin{pmatrix} I \\ Q \\ U \\ V \end{pmatrix} \quad , \tag{1}$$

where

$$\begin{aligned} I &= \langle E_l E_l^* + E_r E_r^* \rangle \quad , \\ Q &= \langle E_l E_l^* - E_r E_r^* \rangle \quad , \\ U &= \langle E_l E_r^* + E_r E_l^* \rangle \quad , \\ V &= i\langle E_l E_r^* - E_r E_l^* \rangle \quad . \end{aligned} \tag{2}$$

Here E_l and E_r are the complex amplitudes of the field referred to a chosen orthonormal system $(\mathbf{e}_l, \mathbf{e}_r)$, see Fig. 1a. They are perpendicular to the direction $\hat{\mathbf{k}}$ of propagation of the wave (i.e., $\hat{\mathbf{k}} \times \mathbf{e}_l = \mathbf{e}_r$), and $\langle \cdot \rangle$ denotes statistical averaging. The Stokes parameters can be measured easily using linear and circular analyzers. Q is determined as the difference between the intensities transmitted through two linear polarizers with orthogonal directions. The parameter U is determined similarly to

Q, but with reference to linear polarizers rotated by 45° with respect to those of Q. Finally V is measured as the difference between the intensities passing through right and left circular analyzers.

The scattered Stokes vector $\mathbf{I}^{(s)}$ is related to the incident Stokes vector $\mathbf{I}^{(i)}$ by the 4×4 scattering matrix F:

$$\mathbf{I}^{(s)} = F\mathbf{I}^{(i)} \ . \tag{3}$$

To determine F we make use of the statistical properties of the fractional permittivity fluctuation $\delta\epsilon(\mathbf{r})$. If it is space-homogeneous and isotropic, its correlation function $R(r)$ is a function of the separation distance r:

$$R(r) = \langle \delta\epsilon(\mathbf{r}')\delta\epsilon(\mathbf{r}' + \mathbf{r}) \rangle \ . \tag{4}$$

The corresponding power spectral density function $\hat{R}(k)$ is a function of the length of the wave vector $\mathbf{k}$:

$$\hat{R}(k) = \frac{1}{(2\pi)^3} \int e^{i\mathbf{kr}} R(\mathbf{r}) d\mathbf{r}. \tag{5}$$

When the correlation length of the fluctuations is small compared with the wavelength, then it is convenient to approximate $R(r)$ by a delta function, $R(r) = R(0)\delta(r)$. Then $\hat{R}(k) = R(0)/(2\pi)^3$.

For weakly fluctuating random media, the scattering matrix is directly related to the power spectral density of the fluctuations by:[23]

$$F(\Theta) = \frac{\pi}{2} k^4 \hat{R}(2k \sin\frac{\Theta}{2}) S(\Theta) \ . \tag{6}$$

Here the scattering angle Θ is the angle between the incident wave vector $\mathbf{k}'$ and the scattered wave vector $\mathbf{k}$, and

$$S(\Theta) = \frac{1}{2} \begin{pmatrix} 1 + \cos^2\Theta & \cos^2\Theta - 1 & 0 & 0 \\ \cos^2\Theta - 1 & 1 + \cos^2\Theta & 0 & 0 \\ 0 & 0 & 2\cos\Theta & 0 \\ 0 & 0 & 0 & 2\cos\Theta \end{pmatrix} \ . \tag{7}$$

The total scattering cross-section $\Sigma_s(k)$ is given in terms of $\hat{R}(k)$ by

$$\Sigma_s(k) = \frac{\pi^2}{2} k^4 \int_{-1}^{1} \hat{R}(k\sqrt{2 - 2\cos\Theta})[1 + \cos^2\Theta] d(\cos\Theta) \ . \tag{8}$$

This form of the scattering matrix (6), involving the power spectral density, comes from the Born expansion of Maxwell's equations in a weakly fluctuating medium. The Born approximation is the single-scattering approximation and its mean intensity (the second moment) must match the single-scattering approximation of the transport equation (34). The mean intensity in the Born approximation is determined by the power spectral density of the fluctuations.

Equation (7) shows that the circularly polarized component V is decoupled from the other components in weakly fluctuating random media, independently of the size of the inhomogeneities. This is because the electric fields scattered from different small volumes within the medium are always independent.[24] This is in clear contrast with the scattering by a medium composed of spherical scatterers with refractive index discontinuities. Then the 4×4 scattering matrix M, derived by Mie theory, is of the form

$$M(\Theta) = \begin{pmatrix} M_{11} & M_{12} & 0 & 0 \\ M_{21} & M_{22} & 0 & 0 \\ 0 & 0 & M_{33} & M_{34} \\ 0 & 0 & M_{43} & M_{44} \end{pmatrix} . \tag{9}$$

The elements M_{34} and M_{43}, which couple the circularly polarized component to the others are in general different from zero. The matrix elements are functions of the the sphere radius, and the relative index of refraction between the spheres and the surrounding medium. When the sphere radius tends to zero, M_{34} and M_{43} tend to zero, and $M(\Theta)$ tends to $S(\Theta)$.

Scattering matrices (7) and (9) are referred to the scattering plane as the plane of reference. The vectors $\mathbf{e}_l$ use to define the incident and scattered Stokes vectors are contained in this plane, see Fig. 1b. In multiple scattering problems, it is more convenient to express (7) with the $\mathbf{e}_l$ parallel to the meridian plane as in Fig. 7. This is discussed in Appendix A where the form of the scattering matrix in this basis is given.

B. Correlation Function and Power Spectral Density Function

Equation (6) is the basic expression for the scattering matrix in a weakly fluctuating random medium, and relates the angular scattering pattern to the statistical characteristics of the medium. The scattering pattern is the product of the matrix $S(\Theta)$, which is a purely geometrical factor, and the scalar function $\hat{R}(2k \sin \Theta/2)$, which involves the statistical properties of the medium. The power spectral density function $\hat{R}$ can be obtained experimentally.[15] However, in many practical situations the spectral characteristics of the fluctuations can be modeled by simple functions. For mathematical simplicity we consider a model with only two parameters: the relative strength of the fluctuations, ε, and the correlation length, l. We use an exponential form for the correlation function,

$$R(r) = \varepsilon^2 e^{-r/l} . \tag{10}$$

In this case the power spectral density function is given by

$$\hat{R}(k) = \frac{\varepsilon^2 l^3}{\pi^2 (1 + k^2 l^2)^2} . \tag{11}$$

The exponential correlation function (10) is a especial case of the von Karman correlation function, used to model the spectral characteristics of the fluctuations in turbulent media.

We note that the power spectral density function (11) becomes independent of k for $kl \ll 1$, so then the factor $\hat{R}$ in (6) is independent of Θ. $\hat{R}(k)$ is proportional to $(kl)^{-4}$ for $kl \gg 1$, so as kl increases, the scattering becomes more peaked in the forward direction.

The mean value of the cosine of the scattering angle, called the anisotropy factor, is defined by

$$g(k) = \frac{\pi^2 k^4}{2\Sigma_s(k)} \int_{-1}^{1} \cos\Theta \hat{R}(k\sqrt{2-2\cos\Theta})[1+\cos^2\Theta]d(\cos\Theta) \ . \qquad (12)$$

It is one of the parameters used to describe the optical properties of a medium. For the correlation function (10) with kl equal to 0, 1, or 2, g is equal to 0, 0.30, or 0.48, respectively. We note that g is typically larger than these values in biological tissues (> 0.70 for wavelengths in the visible). This is so because although the majority of the scattering takes place from structures within the cell, like mitochondria (diameter of the order $0.3 - 0.7\mu m$) or lysomes and peroxisomes (diameter of the order $0.2 - 0.5\mu m$), g is very sensitive to the largest structures of the tissue, that is, to the cell itself (diameter of the order $10 - 30\mu m$).[25,26] More complicated correlation functions than (10) could yield larger values of g for wavelengths in the visible.

To sum up, a tissue is characterized by a power spectral density function $\hat{R}$ which gives the scattering matrix (6), the scattering coefficient (8), and the anisotropy factor (12). The differences between the scattering matrices F and M as the size of the scatterers increases can explain the distinctly different polarization effects reported by Sankaran *et al.*[7] between polarized light propagation in common tissue phantoms (microsphere suspensions) and in biological tissues. Although the phantom is chosen to match the scattering and absorbing properties of the tissue, the high index of refraction ratio between the microspheres and the water alters the polarization effects.

3. Description of the Monte Carlo method

A. Brief review of the literature

Monte Carlo calculations for the study of light propagation in turbid media have been employed by Plass and Kattawar,[27] Meier,[28] Wilson and Adam,[29] Tinet et al.,[30] Zaccanti,[31] and others. In all these papers the vector nature of light propagation was not taken into account. To our knowledge, the first Monte Carlo method which takes into consideration the polarization of light was carried out by Kattawar and Plass.[32] However, in this work the scattering angle is sampled from the scalar phase function, which is the one-one element of the matrix F or M, in (6) or (9), and does

not depend on the polarization state. This scheme is followed by other workers such as, for example, Aruga and Igarashi.[21] If the scalar phase function is used to select the scattering angle, then the light can be scattered in any direction. This is not what happens physically. Since light waves are transverse, they are not emitted along the direction of polarization. Bruscaglioni et al.[33] corrected this by weighting the scattered photon according to the scattering angle and to the incident polarization state. We note that in all these papers[21,32,33] the scattering matrix is defined with respect to the scattering plane as the plane of reference. Consequently, at each scattering event the Stokes vectors, both incident and scattered, have to be rotated appropriately. Since this is time consuming, we express the scattering matrix with respect to the meridian plane as explained in the Appendix.

Partially polarized light is governed by the transport equation (34) for its coherence matrix $W(t, \mathbf{x}, \mathbf{k})$, which is related to the Stokes vector by (33). To solve (34) for W, or for the Stokes vector, we shall use a Monte Carlo method devised especially for this purpose by Bal, Papanicolaou and Ryzhik.[34]

The backbone of a Monte Carlo method for particle transport problems is a simulation of the trajectories of the particles according to underlying probability laws which depend on the scattering medium. The simplest method involves mimicking the random walk of the physical particle transport process and recording a score each time a particle encounters the scoring region. This *analog* simulation, although simple, will be ineffective when few particles reach the scoring region, since the score converges to the expected value at the rate $const./\sqrt{N}$, where N is the number of scores. For problems with an extended source this difficulty can be overcome by using a backward Monte Carlo method, but if the source is a point the difficulty remains.

We use two basic approaches to improve the convergence.[35,36] First, we modify the random walk sampling to follow more particles in *important* regions where the scoring contributes more to the final tally. This is especially relevant in computing light transmission through a medium of large optical thickness. In that case, only a small fraction of particles penetrates in the deeper regions of the medium, producing bad statistics in the computation. Second, we modify the scoring method to maximize the statistical information of a given random walk. In doing this, a trajectory is no longer associated with a single particle. The substitution of the analog simulation by a non-analog one is usually called a *variance reduction technique*.

In the next subsection we describe the simplest case of the analog simulation. In subsection **C** we explain the geometry splitting and Russian roulette, whose objective is to spend more time sampling particles in important regions and less time sampling particles in unimportant regions. In subsection **D** we explain the point detector technique, which is a deterministic estimate of the flux at a point from each collision.

B. Analog Monte Carlo Sampling

The history of each photon is initiated by releasing it from the point $\mathbf{r}_0 = (0,0,0)$ with direction $\hat{\mathbf{k}}_0$ normal to the surface of the medium, and specified polarization state. When the beam is linearly polarized, it is 100% polarized parallel to the (x,z) plane, so the Stokes vector can be written as $[I_0, Q_0, U_0, V_0] = [1,1,0,0]$. When the beam is circularly polarized, the Stokes vector is $[I_0, Q_0, U_0, V_0] = [1,0,0,1]$.

The path length traveled by the photon before undergoing scattering is given by

$$l_{coll} = -ln(\xi)/\Sigma_s \ , \tag{13}$$

where ξ is a random number uniformly distributed in the interval $(0,1)$. Its scattering position $\mathbf{r}_1$ is

$$\mathbf{r}_1 = \mathbf{r}_0 + \hat{\mathbf{k}}_0 l_{coll} \ , \tag{14}$$

with $\hat{\mathbf{k}}_0 = (\sin\theta_0\cos\phi_0, \sin\theta_0\sin\phi_0, \cos\theta_0)$. Next, the scattering direction $\hat{\mathbf{k}}_1$ is determined according to the probability density function[34,37,38]

$$\begin{aligned} P(\hat{\mathbf{k}}_1, \hat{\mathbf{k}}_0, Q_0, U_0) &= \frac{\pi k^4}{2\Sigma_s}\hat{R}\Big[\frac{T_{11}^2 + T_{21}^2 + T_{12}^2 + T_{22}^2}{2} + \frac{T_{11}^2 + T_{21}^2 - T_{12}^2 - T_{22}^2}{2}Q_0 \\ &+ (T_{11}T_{12} + T_{21}T_{22})U_0\Big] \ . \end{aligned} \tag{15}$$

Equation (15) corresponds to the first component of $\mathbf{I}^{(s)}$ in equation (3) when the intensity of the incident Stokes vector $\mathbf{I}^{(i)}$ is normalized to one. The probability density function P also contains a normalization factor to preserve particle number in a pure scattering event. This normalization factor is independent of the incoming state of polarization.

In (15), $T_{ij}, (i,j = 1,2)$ is defined in Appendix A. P has been normalized to satisfy

$$\int P(\hat{\mathbf{k}}_1, \hat{\mathbf{k}}_0, Q_0, U_0) d\hat{\mathbf{k}}_1 = 1 \ , \tag{16}$$

and the argument of $\hat{R}$ is $k|\hat{\mathbf{k}}_1 - \hat{\mathbf{k}}_0| = 2k\sin\frac{\Theta}{2}$. Equation (16) expresses particle conservation in each scattering event. We note that P in (15) depends on the incidence and scattering directions, and also on the incoming polarization state. We also note that in (16), the integral of the terms multiplied by Q_0 and U_0 is zero. Once the new direction $\hat{\mathbf{k}}_1$ is chosen, the outgoing polarization state is

$$\mathbf{I}^{(1)} = \frac{1}{\Sigma_s P(\hat{\mathbf{k}}_1, \hat{\mathbf{k}}_0, Q_0, U_0)}\bar{F}(\hat{\mathbf{k}}_1, \hat{\mathbf{k}}_0)\mathbf{I}^{(0)} \ . \tag{17}$$

This does not depend on $\hat{R}(k)$. In (17) $\bar{F}$ is the scattering matrix with the meridian plane as plane of reference for the Stokes vectors. It can be checked by direct computation that if the incident photon is fully polarized, i.e. $I_0^2 = Q_0^2 + U_0^2 + V_0^2$,

then the scattered photon, with polarization $\mathbf{I}^{(1)}$ given by (17), is also completely polarized.

Next, a new path length is calculated from (13) and the tracing continues using (14)-(17), where now sub-indices 0 and 1 denote the variables of the photon before and after each scattering event, respectively.

If a photon reaches the detector at an angle with the normal to the sample surface that is less than its semiaperture, then its contribution to the quantities of interest (intensity and polarization) are stored. If the incident beam is circularly polarized, two quantities are computed: the total intensity I and the circular component V. In the case of a linearly polarized incident beam, three intensities are computed: the total intensity I, the parallel-polarized component I_l, and the cross-polarized component I_r. If a photon of intensity $dI = 1$ arrives at the detector with polar direction (θ_d, ϕ_d), these two last intensities can be calculated easily from the Stokes parameters Q_d and U_d of the photon. The direction of polarization makes an angle $\chi_d = 1/2 \arctan(U_d/Q_d)$ with the meridian plane (plane of constant ϕ_d), and therefore the contribution of the photon is:

$$I = dI \ , \tag{18}$$

$$I_l = dI[\cos^2(\phi_d + \chi_d)\cos^2\theta_d + \sin^2\theta_d] \ , \tag{19}$$

$$I_r = dI[\sin^2(\phi_d + \chi_d)\cos^2\theta_d + \sin^2\theta_d] \ . \tag{20}$$

Here we are interested in the transmitted intensity. To compute the reflected intensity, we must change χ_d to $-\chi_d$ in equations (19) and (20).

After N photons have been traced, and the intensities $I^{(n)}$, $I_l^{(n)}$, $I_r^{(n)}$, and $V^{(n)}$ of the N histories have been stored, we average to obtain the statistical result,

$$\bar{I} = \frac{1}{N}\sum_{n=1}^{N} I^{(n)}, \quad \bar{I}_l = \frac{1}{N}\sum_{n=1}^{N} I_l^{(n)}, \quad \bar{I}_r = \frac{1}{N}\sum_{n=1}^{N} I_r^{(n)}, \quad \bar{V} = \frac{1}{N}\sum_{n=1}^{N} V^{(n)} \ . \tag{21}$$

We note from (19) and (20) that $I_l + I_r = I(1 + \sin^2\theta_d)$. This is not equal to I unless $\sin\theta_d = 0$, because if $\sin\theta_d \neq 0$ there is a component of the electric field normal to the analyzers. This component is transmitted through them independently of their orientation. Consequently, when measuring a bundle of light, in a typical experimental situation, the sum $\bar{I}_l + \bar{I}_r$ of the parallel and cross-polarized components is not equal to the total intensity $\bar{I}$, measured without polarization analyzers.

We also note that the fraction of light with the original polarization, $(\bar{I}_l - \bar{I}_r)/\bar{I}$, coincides with the common definition of the degree of polarization $\sqrt{\bar{Q}^2 + \bar{U}^2}/\bar{I}$, only for small apertures. In this case, the intensity of light that has maintained the incident polarization state, $\bar{I}_l - \bar{I}_r$, is a measure of the Stokes parameter $\bar{Q}$, and $\bar{U}$ is zero due to the symmetry of the problem.

C. Splitting and Russian Roulette

One of the most widely used variance reduction methods is the combination of the so called importance splitting and Russian roulette techniques. The problem domain is divided into M subdomains with different importances $\mathcal{I}^{(m)}$ $(m = 0, \ldots, M-1)$. We will assume for simplicity that $\mathcal{I}^{(m)} = c^m$ where c is a chosen positive integer. The more probable it is that a particle in a sub-domain can score at the detector, the more important is the sub-domain. Let a particle of weight W evolve between two collisions i and $i+1$, and let us denote the importance of the particle by $\mathcal{I}_i$ and $\mathcal{I}_{i+1}$ at each collision ($\mathcal{I}_i = \mathcal{I}^{(m)}$ if at collision i the photon is in sub-domain m). We form the importance ratio $\eta = \mathcal{I}_{i+1}/\mathcal{I}_i$. If $\eta = 1$ the importance of the photon does not change and its transport continues in the usual way. If $\eta > 1$ the photon has moved to a more important region and it is split into $N_{split} = \eta$ photons. The weight W of each of the split photons is divided by N_{split}. If $\eta < 1$ it has entered into a less important region, and a Russian roulette game is played where the particle has probability $p_{surv} = \eta$ of surviving. A random number ξ is drawn uniformly on the interval $(0, 1)$ and compared with p_{surv}. If $\xi < p_{surv}$ the photon survives and its weight is increased by $1/p_{surv}$. Otherwise, it is eliminated. In doing this, however, a balance has to be struck. Implementing splitting generally decreases the history variance but increases the computing time per history. On the contrary, Russian roulette increases the former and decreases the latter, so that more histories can be run. The usual measure of efficiency of the Monte Carlo simulations is the figure of merit $1/\sigma^2 t$, where the variance σ^2 measures the inaccuracy of the result, and t is the mean time per history. We have seen experimentally that, for example, for a medium of optical thickness 12, the choice $c = 2$ and $M = 5$ improves the figure of merit by a factor 10. However, for optical thickness less than 8 we have not found the splitting/Russian roulette necessary. For deep penetration, experience has indicated that the best splitting results are achieved keeping the particle flux through the medium close to a flat distribution, and that there is a broad range of parameters close to the optimal choice.[36] If splitting with Russian roulette is the only variance reduction technique used, all particles in the same sub-domain m have the same weight $1/\mathcal{I}^{(m)}$, assuming that all particle histories began with weight 1.

D. Point detectors

We now consider scoring at a small detector of area dA, often called a *point detector*. For each scattering event i of the n-th photon, we store the probability that the n-th scattered photon, of weight $W_i^{(n)}$, will arrive at the detector without further collisions. Let $P(\Theta, \mathcal{P})d\Omega$ be the probability of scattering into the solid angle $d\Omega$ about Θ, where Θ is the scattering angle directed to the detector, and $\mathcal{P} = (Q_0, U_0)$ denotes the liner polarization state of the photon. Taking into account the attenuation suffered by particles traveling through the medium, the probability of arriving at

the detector is

$$P(\Theta,\mathcal{P})d\Omega e^{-\int_0^R \Sigma_s(l)dl} \ , \tag{22}$$

where R is the distance covered within the medium. We recall that we are considering non-absorbing media. Absorption can be accounted for easily by replacing the scattering coefficient Σ_s in (22) by the total extinction coefficient $\Sigma_t = \Sigma_s + \Sigma_a$, where Σ_a is the absorption coefficient.

If the detector of area dA has normal vector forming the angle θ_d with respect to the line of flight, then $d\Omega = \cos\theta_d dA/R^2$, and (22) becomes

$$P(\Theta,\mathcal{P})\frac{\cos\theta_d e^{-\int_0^R \Sigma_s(l)dl}}{R^2}dA \ . \tag{23}$$

Since the flux is the number of particles crossing per unit area and per unit time, the contribution of the i-th collision to the flux at the detector is given by

$$\mathcal{F}_{Ii}^{(n)} = W_i^{(n)} P(\Theta,\mathcal{P})\frac{\cos\theta_d e^{-\Sigma_s R}}{R^2} \ . \tag{24}$$

Here we have evaluated the integral for a homogeneous medium. The contribution to the Stokes parameters is given by equation (17) times $\mathcal{F}_{Ii}^{(n)}$. In the case of a linearly polarized incident beam, the contributions to the parallel and cross-polarized components are evaluated with expressions similar to (19) and (20), respectively.

After N photons have been traced, the statistical averages are computed as

$$\bar{\mathcal{F}}_I = \frac{1}{N}\sum_{n=1}^{N}\sum_{i=1}^{S_n}\mathcal{F}_{Ii}^{(n)}, \quad \bar{\mathcal{F}}_l = \frac{1}{N}\sum_{n=1}^{N}\sum_{i=1}^{S_n}\mathcal{F}_{li}^{(n)}, \quad \bar{\mathcal{F}}_r = \frac{1}{N}\sum_{n=1}^{N}\sum_{i=1}^{S_n}\mathcal{F}_{ri}^{(n)}, \quad \bar{\mathcal{F}}_V = \frac{1}{N}\sum_{n=1}^{N}\sum_{i=1}^{S_n}\mathcal{F}_{Vi}^{(n)} \ , \tag{25}$$

where S_n is the number of scatterings events of the n-th photon.

In spite of the simplicity of the method, the point detector estimator has a serious drawback. The expression (24) becomes infinite when a collision takes place infinitely close to the detector, giving rise to an unbounded estimator with infinite variance and consequently a low rate of convergence. Several methods have been developed to overcome this difficulty.[39–41] However, if the detector is not in the scattering medium, a collision close to the detector is impossible and the estimator is bounded. Our point detectors are placed at a distance $d = 1mm$ from the exit surface, so we replace the R in the denominator of Eq. (24) by $(R + d/\cos\theta_d)$. Point detectors have been used widely in the literature.[30,33,39,42] In the paper of Tinet et al.[30] point detectors are used along with the statistical estimator idea to accelerate the convergence for scalar transport.

Since tracing photons from each collision to the detector is time consuming, especially in the case where an object is embedded, we have also implemented a Russian roullete game for the detector. If the collision takes place in a region of

importance $\mathcal{I}^{(m)}$, we introduce the probability to contribute to the flux equal to $\mathcal{I}^{(m)}/\mathcal{I}^{(M-1)} = c^{m-M+1}$. If the particle wins the game its deterministic contribution is multiplied by $\mathcal{I}^{(M-1)}/\mathcal{I}^{(m)}$ and it is stored. Otherwise, the contribution is not stored.

4. Numerical Results

A. Scan profiles with barrier

Figure 2a shows the geometry of our numerical experiment. A normally incident linearly polarized laser beam is used to illuminate an $8mm \times 8mm \times 8mm$ sample. The different laser beam positions at the top of the sample are $0.5mm$ apart. A single measurement is made by placing the laser beam at one of these positions and the detector on the optical axis at the bottom of the sample. The detector collects transmitted photons with polarization parallel and perpendicular to the incident polarization, at angles less than 16° from the normal to the sample surface. In the middle of the sample there is a $2mm \times 8mm$ absorbing strip. A complete scan consists of 9 measurements. This configuration is motivated by the experiments of Schmitt et. al..[12] The same results are obtained for similarly scaled geometries if the optical thickness of the medium, $\tau = \Sigma_s Z$, is kept constant and the media are non-absorbing. For microsphere suspensions, the mean free path Σ_s^{-1} depends on the scatterer concentration and is in the range $4 - 200mm$ in some recent experiments measuring polarization.[7,12,14] However, biological tissues have smaller mean free paths, of the order of $0.03 - 0.2mm$. Therefore the thickness of the sample Z must be adjusted so that its optical depth is not so big that the polarization cannot be measured. Scattering mean free paths of other media are shown in table 1. Our numerically computed intensity and polarization are shown as functions of the optical thickness. Table 1 can then be used to determine corresponding distances for imaging in different scattering media.

In Figs. 3a and 3b we show scan profiles for samples of optical thickness $\tau = 4$ and $\tau = 9$, respectively. In both cases the correlation length of the random inhomogeneities is much smaller than the incident wavelength ($kl \ll 1$). The solid curve is the calculated profile of the total transmitted intensity I. The dashed curve is the calculated profile for the polarization-difference, obtained by subtracting the perpendicular transmitted component I_r from the parallel transmitted component I_l. The thick line at the top of the figure indicates the position of the absorbing strip. The profiles have been normalized by their maxima. For $\tau = 4$, both the total intensity profile and the polarization-difference profile resolve the barrier, and the polarization-difference technique does not have any particular advantage. However, for $\tau = 9$ the enhanced resolution of the polarization-difference technique is apparent. The reason for this enhanced resolution is that the subtraction of one orthogonal polarized component from the other cancels the diffusive component of the trans-

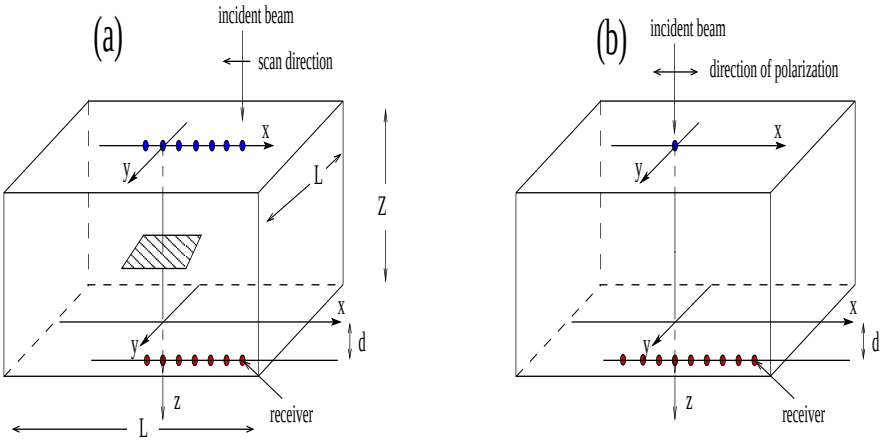

Fig. 2. The setup used in the numerical simulations. (a) The sample is an $8mm$ cube, so $L = Z = 8mm$. It contains a $2mm \times 8mm$ opaque absorbing plate. The distance between two consecutives incident beam positions is $0.5mm$. The detectors are placed at a distance $d = 1mm$ from the exit surface. The width of the incident laser beam, measured at $1/e$ of the maximum, is $0.5mm$. (b) Geometry used for the numerical computation of the point-spread functions. The incident beam, impinging on $(x, y) = (0, 0)$, has zero width. The detector positions are $0.2mm$ apart.

mitted light. In the difference $I_l - I_r$, only ballistic photons and weakly scattered photons (snake photons), which keep their initial polarization, are retained.

Another consequence of the subtraction of one polarization from the other is that the un-normalized scan profile of the polarization-difference $I_l - I_r$ is smaller than the un-normalized scan profile of the total intensity I. For example, for $\tau = 9$ the polarization-difference has decreased by a factor of 16 compared to I, see Fig. 6a. We comment further on this in subsection **4C**.

This example clearly shows that the polarization-difference technique can enhance the image quality of an embbeded target in highly scattering media. Although this problem has been treated in the literature, none of the studies has considered polarization discrimination in continuous random media.

Next we study this phenomenon as a function of the ratio of the correlation-length of the inhomogeneities to the incident wavelength, and its dependence on the incident polarization state and on the aperture of the receiver. All these questions will be treated in terms of the point-spread functions.

B. Point-spread functions

Now we consider light from a very narrow parallel beam impinging normally on the sample. We compute the transmitted profiles of the intensity I, of the polarization-

Type of medium	$(\Sigma_s)^{-1}$	Reference
Porcine Fat	0.15 mm	Cheong[43]
Aorta (human)	0.03 mm	
Fog and Clouds	25 - 500 m	McCartney[44]
Haze	0.5 - 2 Km	
Clear weather	2 - 12 Km	
Pure air	70 Km	
Pure water	25 - 100 m	Ishimaru[24]
Sea-water(only due to particulate matter)	3.3 m	

Table 1. Typical mean free paths of visible light in different media.

difference $I_l - I_r$, and of the degree of polarization $(I_l - I_r)/I$ at points on the output face of the sample, see Fig. 2b. These results correspond to the point-spread functions measured in experimental situations. In our simulations, the different detector positions are $0.2mm$ apart.

If the medium is completely homogeneous there is no scattering and the measured profile of the intensity is a delta function. On the other hand, if the medium is not homogeneous, the light interacts with the inhomogeneities and the beam is spread as it propagates through the sample. This results in image blurring. However, the spread of other measurable quantities like the polarization-difference or the degree of polarization does not have to behave similarly.

In Figure 4 we show three typical point-spread functions for a sample of optical thickness $\tau = 9$, with $kl \ll 1$ and a receiver semiaperture of 16°. The solid line is the intensity I, the dashed line is the polarization-difference $I_l - I_r$, and the dot-dashed line is the degree of polarization $(I_l - I_r)/I$. Images in different systems have been studied using this quantity.[7,11,45] Again, for ease of comparison, all curves in Fig. 4 have been normalized to their maximum values at the optical axis. The maximum value for the degree of polarization is shown in Fig. 6a. Figure 4 shows that, in this case, the best spatial resolution and contrast will be achieved by the polarization difference image, $I_l - I_r$. This explains why the polarization difference yielded the improvement observed in Fig. 3b.

To describe quantitatively the enhancement due to the polarization-difference

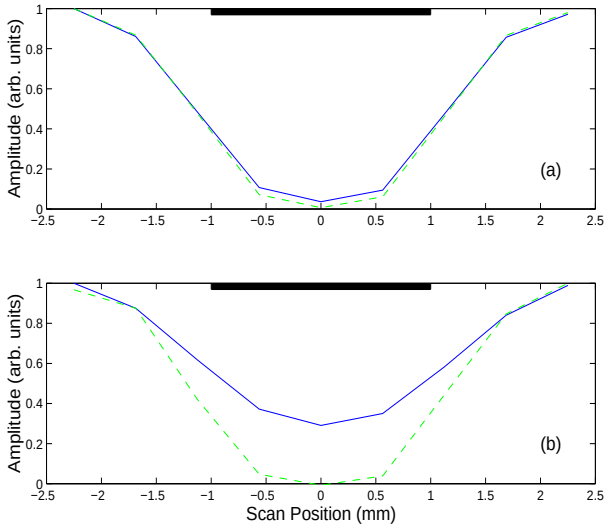

Fig. 3. Numerical results for scan profiles with (a)$\tau = 4$ and (b)$\tau = 9$. The solid line is the computed total intensity and the dashed curve is the computed polarization-difference. All curves are normalized to their maximum values. The semiaperture angle of the receiver is 16° and the width of the incident beam is $0.5mm$. The thick line at the top of the figure represents the position of the absorbing strip.

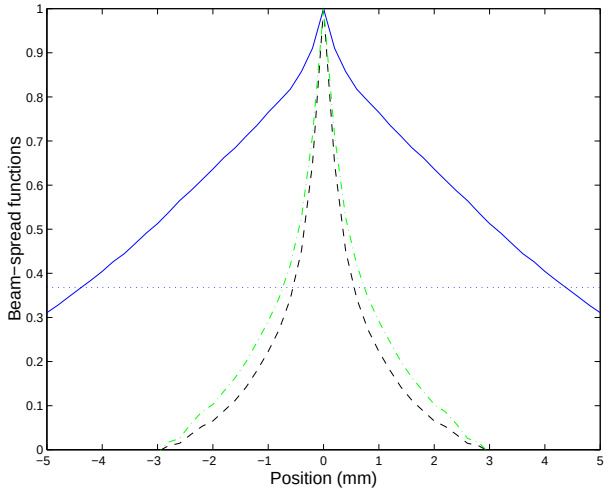

Fig. 4. The point-spread functions in the $x - z$ plane. The normally incident beam is 100% linearly polarized parallel to this plane. Solid line, dashed line, and dot-dashed line are the total intensity, the polarized difference intensity, and the polarized difference intensity divided by the total intensity, respectively. The spatial profiles are calculated at the bottom of the sample, see Fig. 2b. The optical thickness $\tau = 9$, the semiaperture angle of the receiver is 16°, and $kl \ll 1$. All curves are normalized to their maximum values at $x = 0$. The horizontal dotted line is the value $1/e$.

we show in Fig. 5a the half-width of the point-spread functions at $1/e$ of their maxima (horizontal dotted line in Fig. 4) as functions of the optical thickness. Open circles represent total intensity, open diamonds polarization-difference, and open squares degree of polarization. The half-widths for a circularly polarized incident beam are shown also. In this case the discrimination of short-path photons is based on the circularly polarized component V of the output beam, and the polarization-sensitive point-spread function is simply V (solid diamonds). As in the case of a linearly polarized beam, we also represent the half-width of the profile of degree of polarization, i.e. of V/I (solid squares). Solid circles represent the half-width corresponding to the transmitted intensity when the incident beam is circularly polarized. The main features of this figure are:

(i) The width of the point-spread function of the polarization-difference is the smallest of the three for all optical thicknesses.

(ii) The width of the point-spread function of the polarization-difference is the same as the width of the point-spread function of the intensity for small optical thicknesses, and it is the same as the width of the degree of polarization for large optical thicknesses. The error of our calculations is equal to the separation of the detectors, which is $0.2mm$.

(iii) There is a critical depth ($\tau = 5$ in this case) where the broadening of the point-spread function of the intensity grows exponentially.

(iv) The width of the point-spread function of the polarization-difference remains constant for increasing optical thickness, at least for $\tau \leq 14$.

(v) The widths of the point-spread functions do not depend on whether the light incident upon the sample is linearly or circularly polarized.

Figure 5b shows half-widths of the point-spread functions when the receiver collects photons at all angles. In this case, multiple scattering results in blurring of the image which degrades the point-spread function of the intensity even for very small optical depths, and the benefit of polarization-difference imaging is even more important. This is an expected result because the larger the aperture, the larger the ratio between the number of diffusive photons and ballistic and snake photons. Another difference from Fig. 5a is worth pointing out. Polarization discrimination of ballistic and snake photons based on circularly polarized light gives rise to a wider point-spread function than that of the one based on linearly polarized light. Therefore, the spatial resolution achieved with linearly polarized light will be better if large apertures are used.

In media with correlation-lengths of the order of the incident wavelength ($kl = 1$) or larger ($kl = 2$) we have obtained similar results (not shown) except that the

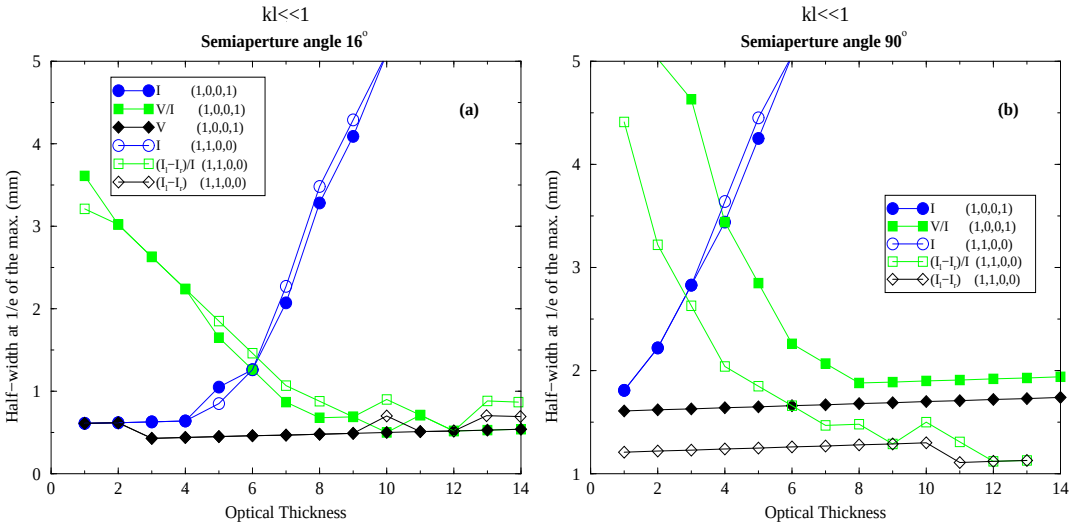

Fig. 5. Beam half-width at $1/e$ of the maximum (in mm) of the point-spread functions. Solid and open symbols are for circularly $[(1,0,0,1)]$ and linearly $[(1,1,0,0)]$ polarized incident light, respectively. Circles, diamonds, and squares are for total intensity, polarized difference intensity, and polarized difference intensity divided by the total intensity, respectively. $kl = 1$. (a) semiaperture angle of the receiver 16°, and (b) semiaperture angle of the receiver 90°.

critical depth at which the width of the point-spread function of the intensity starts to increase was larger. For $kl = 1$ and semiaperture angles of 16° and 90° the critical depths were 8 and 4, respectively. For $kl = 2$ they were 10 and 7. We have also found that above this critical depth the width of the point-spread function of the intensity increased more rapidly than for $kl \ll 1$.

We note that, in contrast to our results for weakly fluctuating random media, when a circularly polarized laser beam is incident upon a medium containing spheres of large diameter, the spreading of the transmitted polarized component V and the total intensity I are similar (see Fig. 6 in reference 12). Consequently, circularly polarized light cannot be use to discriminate between weakly and strongly scattered photons in these cases.

C. Maximum of the degree of polarization

The polarization-difference yields a better image than the total intensity, but it is also weaker. To see how much weaker it is, we consider the polarization fraction, i.e. the degree of polarization, as a function of the optical thickness. Fig. 6 shows, on a semilogarithmic scale, the dependence of the maximum of the point-spread function of the degree of polarization on the optical thickness for different values of kl and for

small and large detector apertures. These values with table 1 provide an estimate of the maximum distance Z_{max} through which polarization-sensitive techniques can image abnormal targets within the medium. Let τ_{lim} be the optical depth at which the minimum possible detected value of the degree of polarization is reached. Then, Z_{max} is equal to τ_{lim}/Σ_s, where Σ_s is the scattering coefficient of the medium.

Fig. 6 shows that for small detector apertures, independently of kl, the maximum the degree of polarization for both incident polarization states (linear and circular) decay at the same rate as the optical thickness increases. This agrees with results of Sankaran *et al.*,[7] who use a semiaperture of 13°, for fat and artery tissue and for polystyrene suspensions of small diameter. We recall that for small diameter scatterers, the single scattering matrix coincides with the scattering matrix of a random medium with $kl \ll 1$.

Sankaran *et al.*[7] and others[12,17] also found that as the particle size increased, circularly polarized light became much less depolarized than linearly polarized light. The reason is that there is a critical scattering angle, above which the helicity of a circular polarized photon is reversed and below which it is preserved. For spherical scatterers, this helicity flip angle increases with the size of the scatterers and therefore, for large-diameter spheres, off-axis scattered photons also maintain their original polarization after scattering. This explanation led in Schmitt et. al.[12] to the hypothesis that short-path photons propagating in biological tissues with large anisotropy factors can be better selected by using linearly polarized incident light. However, in weak random media the critical helicity flip angle is always equal to 90°. We find that circularly polarized light is significantly less depolarized than linearly polarized light only for $kl > 2$ and large apertures. See Fig. 6.

We note that the slopes in Fig. 6 do not depend on the detector aperture, and that they decrease (in absolute value) as kl increases.

5. Conclusions

We have presented numerical simulations for light propagation in biological tissues based on the theory of wave propagation in continuous random media. With this theory we can explain why depolarization is different in biological tissues from that for propagation through phantom tissues composed of microsphere suspensions. That is because they have different scattering matrices in the transport equation for the Stokes parameters as explained in section 2. We note also that although the anisotropy parameter g of a microsphere suspension can be adjusted to match the observed intensity of light through biological tissue, the polarizations will differ in general.

Using a Monte Carlo method we solve a system of radiative transport equations for the components of the Stokes vector. The results demonstrate that polarization-sensitive techniques can produce less blurred images. They do so by discriminating ballistic and snake photons form diffusive photons. We have studied the depolariz-

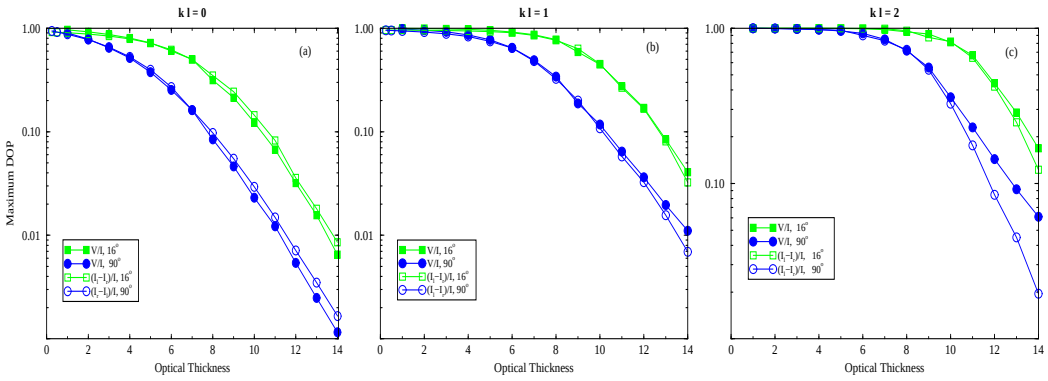

Fig. 6. Maximum degree of polarization for media with (a) $kl = 0$, (b) $kl = 1$, and (c) $kl = 2$. Solid and open symbols are for circularly and linearly polarized incident light, respectively. Squares and circles are for semiapertures of the receiver equal to 16° and 90°, respectively. The relative standard error is less than 0.01.

ation and blurring of images by computing the point-spread functions for different initial polarization states, different optical thickness, and different apertures of the receivers.

Our main result is that in weakly fluctuating random media, discrimination based on polarization measurements is better than polarization-blind methods. This is true, regardless of the initial polarization state of the laser beam, for all optical thicknesses and all correlation lengths of the fluctuations. This agrees with the experimental results of Sankaran et al.[7] which showed that linear polarization does not have advantages over circular polarization for imaging through fat and artery tissues. Our results contrast with those in microsphere suspensions. In them, circular polarization techniques improve the detectability of an embedded object only for relatively small scatterer sizes.

Acknowledgment

This work was supported by AFOSR grant 49620-98-1-0211 and by NSF grant 9709320.

A Radiative transfer theory

The electric vector $\mathbf{E}(\mathbf{x}, t)$ of a monochromatic wave has components in two orthogonal directions $\mathbf{e}_1$ and $\mathbf{e}_2$ perpendicular to the wave vector $\mathbf{k}$, see Fig.1a. Its polarization can be characterized by the end point of an arrow representing the wave motion, which describes an ellipse with unequal principal axes as t varies. If

$(\mathbf{e}_1, \mathbf{e}_2)$ are chosen in the direction of the principal axes, then

$$\mathbf{E}(t, \mathbf{x}) = \mathbf{e}_1 E_1^0 \cos(\omega t - \mathbf{kx} + \alpha) + \mathbf{e}_2 E_2^0 \sin(\omega t - \mathbf{kx} + \alpha) \quad . \tag{26}$$

In complex form,

$$\mathbf{E}(t, \mathbf{x}) = \mathbf{E} e^{-i(\omega t - \mathbf{kx} + \alpha)} + \mathbf{E}^* e^{i(\omega t - \mathbf{kx} + \alpha)} \quad , \tag{27}$$

where

$$\mathbf{E} = E^0(\mathbf{e}_1 \cos\beta + i\mathbf{e}_2 \sin\beta). \tag{28}$$

In (26) and (27), ω is the frequency, E_1^0, E_2^0, E^0 and α are constants, and β is the angle (between 0 and $\pi/2$) whose tangent is the ratio of the principal axes of the ellipse.

If $\mathbf{E}$ is expanded in some other general directions $(\mathbf{e}_l, \mathbf{e}_r)$ making angles χ and $\pi/2 - \chi$ with the direction $\mathbf{e}_1$, then

$$\mathbf{E}(t, \mathbf{x}) = E_l \mathbf{e}_l + E_r \mathbf{e}_r \quad , \tag{29}$$

with

$$\begin{aligned} E_l &= E^0(\cos\chi\cos\beta - i\sin\chi\sin\beta) \\ E_r &= E^0(\sin\chi\cos\beta + i\cos\chi\sin\beta) \quad . \end{aligned} \tag{30}$$

Light can be described by time averages of quadratic combinations of the field components. A convenient combination of them is the 2×2 coherence matrix,

$$W(t, \mathbf{x}, \mathbf{k}) = \begin{pmatrix} \langle |E_l|^2 \rangle & \langle E_l E_r^* \rangle \\ \langle E_l^* E_r \rangle & \langle |E_r|^2 \rangle \end{pmatrix}. \tag{31}$$

This matrix completely describes the light intensity and polarization. The common practice is to characterize these properties by the four Stokes parameters,

$$\begin{aligned} I &= \langle E_l E_l^* + E_r E_r^* \rangle = I_l + I_r, \\ Q &= \langle E_l E_l^* - E_r E_r^* \rangle = I_l - I_r, \\ U &= \langle E_l E_r^* + E_r E_l^* \rangle = [I_l - I_r]\tan 2\chi, \\ V &= i\langle E_l E_r^* - E_r E_l^* \rangle = [I_l - I_r]\tan 2\beta \sec 2\chi. \end{aligned} \tag{32}$$

With these definitions,

$$W(t, \mathbf{x}, \mathbf{k}) = \frac{1}{2}\begin{pmatrix} I + Q & U - iV \\ U + iV & I - Q \end{pmatrix}. \tag{33}$$

In a weakly inhomogeneous random medium, W satisfies the transport equation[23]

$$\frac{1}{v}\frac{\partial W(t, \mathbf{x}, \mathbf{k})}{\partial t} + \hat{\mathbf{k}} \cdot \nabla_{\mathbf{x}} W(t, \mathbf{x}, \mathbf{k}) = \int \sigma(\mathbf{k}, \mathbf{k}')[W(\mathbf{k}')]d\mathbf{k}' - \Sigma(\mathbf{k})W(t, \mathbf{x}, \mathbf{k}). \tag{34}$$

Here v is the propagation velocity in the uniform background medium. This equation has to be solved with appropriate boundary conditions. Suppose that a very narrow normally incident laser beam, with normalized intensity 1, 100% polarized along the plane $x-z$ is incident at $\rho_0 = \sqrt{x_0^2 + y_0^2} = 0$, on the plane boundary $z = 0$ of the medium. Then

$$W(0, \rho, z = 0, \mathbf{k}) = \begin{pmatrix} 1 & 0 \\ 0 & 0 \end{pmatrix} \frac{1}{2\pi\rho} \delta(\rho)\delta(\mathbf{k} - \mathbf{k}_0) \tag{35}$$

with $\mathbf{k}_0 = (0, 0, 1)$. If the laser beam is circularly polarized the matrix in (35) is replaced by

$$\frac{1}{2}\begin{pmatrix} 1 & -i \\ i & 1 \end{pmatrix} \quad . \tag{36}$$

For the simplest case of isotropic random inhomogeneities, without fluctuations in the magnetic permeability, the differential scattering tensor has the form,

$$\sigma(\mathbf{k}, \mathbf{k}')[W(\mathbf{k}')] = \bar{\sigma} T(\mathbf{k}, \mathbf{k}') W(\mathbf{k}') T^*(\mathbf{k}, \mathbf{k}') \delta(|\mathbf{k}| - |\mathbf{k}'|) \quad , \tag{37}$$

where

$$\bar{\sigma} = \frac{\pi}{2} |\mathbf{k}|^2 \hat{R}(|\mathbf{k} - \mathbf{k}'|) \quad , \tag{38}$$

is a scalar function which depends on the spectral power density of the permittivity fluctuation. The second power of $|\mathbf{k}|$ in this expression becomes the fourth power as in (6) when we use polar coordinates. The 2×2 matrix $T(\mathbf{k}, \mathbf{k}')$ is defined by

$$T_{ij}(\mathbf{k}, \mathbf{k}') = \mathbf{z}^{(i)}(\mathbf{k}) \cdot \mathbf{z}^{(j)}(\mathbf{k}') \qquad i, j = 1, 2 \ . \tag{39}$$

The vectors $(\hat{\mathbf{k}}, \mathbf{z}^{(1)}(\mathbf{k}), \mathbf{z}^{(2)}(\mathbf{k}))$,

$$\hat{\mathbf{k}} = \begin{pmatrix} \sin\theta\cos\phi \\ \sin\theta\sin\phi \\ \cos\theta \end{pmatrix}, \ \mathbf{z}^{(1)}(\mathbf{k}) = \begin{pmatrix} \cos\theta\cos\phi \\ \cos\theta\sin\phi \\ -\sin\theta \end{pmatrix}, \ \mathbf{z}^{(2)}(\mathbf{k}) = \begin{pmatrix} -\sin\phi \\ \cos\phi \\ 0 \end{pmatrix}, \tag{40}$$

form a local right-handed orthonormal basis in $I\!R^3$, see Fig. 7. It is important to emphasize that the Stokes parameters are defined with respect to a plane of reference passing through the direction of propagation $\hat{\mathbf{k}}$. Above, we have defined the differential scattering tensor with respect to the meridian plane defined by the vectors $\hat{\mathbf{k}}$ and $\mathbf{z}^{(1)}(\hat{\mathbf{k}})$.

The delta function in Eq. (37) implies that the frequency $\omega = v|\mathbf{k}|$ is unchanged by scattering, since (37) is valid for time-independent fluctuations. The differential scattering tensor (37) and the total scattering cross section $\Sigma(\mathbf{k})$ are related by

$$\int_{I\!R^3} \sigma(\mathbf{k}', \mathbf{k})[I\!I_2] d\mathbf{k}' = \Sigma(\mathbf{k}) I\!I_2 \ , \tag{41}$$

where $\mathbb{I}_2$ is the 2×2 identity matrix, and

$$\Sigma(\mathbf{k}) = \frac{\pi^2 |\mathbf{k}|^4}{2} \int_{-1}^{1} \hat{R}(|\mathbf{k}|\sqrt{2-2\cos\Theta})[1+\cos^2\Theta] d(\cos\Theta) \ . \tag{42}$$

Here, $\cos\Theta = \hat{\mathbf{k}} \cdot \hat{\mathbf{k}}'$.

Let us now write the radiative transfer equation (34) in terms of the 4×1 Stokes vector

$$\mathbf{I} = \begin{pmatrix} I \\ Q \\ U \\ V \end{pmatrix} \ , \tag{43}$$

instead of the 2×2 coherence matrix W. We have to replace the 2×2 scattering tensor (37) by a 4×4 matrix F, so that

$$\mathbf{I}^{(s)} = F \mathbf{I}^{(i)} \ , \tag{44}$$

where $\mathbf{I}^{(i)}$ and $\mathbf{I}^{(s)}$ are the incident and scattered Stokes vectors, respectively. Straight matrix multiplication gives,

$$TWT^* = \frac{1}{2} T \begin{pmatrix} I^{(i)} + Q^{(i)} & U^{(i)} - iV^{(i)} \\ U^{(i)} + iV^{(i)} & I^{(i)} - Q^{(i)} \end{pmatrix} T^* = \frac{1}{2} \begin{pmatrix} A & B - iC \\ B + iC & D \end{pmatrix} \tag{45}$$

with,

$$\begin{aligned}
A &= [T_{11}^2 + T_{12}^2] I^{(i)} + [T_{11}^2 - T_{12}^2] Q^{(i)} + 2T_{11}T_{12} U^{(i)} && (46) \\
B &= [T_{11}T_{21} + T_{12}T_{22}] I^{(i)} + [T_{11}T_{21} - T_{12}T_{22}] Q^{(i)} + [T_{11}T_{22} + T_{12}T_{21}] U^{(i)} && (47) \\
C &= [T_{11}T_{22} - T_{12}T_{21}] V^{(i)} && (48) \\
D &= [T_{21}^2 + T_{22}^2] I^{(i)} + [T_{21}^2 - T_{22}^2] Q^{(i)} + 2T_{21}T_{22} U^{(i)} \ . && (49)
\end{aligned}$$

We easily identify the scattered Stokes parameters from (45) as $I^{(s)} = \bar{\sigma}(A + D)/2$, $Q^{(s)} = \bar{\sigma}(A - D)/2$, $U^{(s)} = \bar{\sigma} B$, and $V^{(s)} = \bar{\sigma} C$, so that

$$\begin{aligned}
I^{(s)} &= \bar{\sigma} \tfrac{1}{2} \{ [T_{11}^2 + T_{12}^2 + T_{21}^2 + T_{22}^2] I^{(i)} + [T_{11}^2 + T_{21}^2 - T_{12}^2 + T_{22}^2] Q^{(i)} + 2[T_{11}T_{12} + T_{21}T_{22}] U^{(i)} \} \ , \\
Q^{(s)} &= \bar{\sigma} \tfrac{1}{2} \{ [T_{11}^2 + T_{12}^2 - T_{21}^2 - T_{22}^2] I^{(i)} + [T_{11}^2 + T_{22}^2 - T_{12}^2 - T_{21}^2] Q^{(i)} + 2[T_{11}T_{12} - T_{21}T_{22}] U^{(i)} \} \ , \\
U^{(s)} &= \bar{\sigma} [T_{11}T_{21} + T_{12}T_{22}] I^{(i)} + [T_{11}T_{21} - T_{12}T_{22}] Q^{(i)} + [T_{11}T_{22} + T_{12}T_{21}] U^{(i)} \ , \\
V^{(s)} &= \bar{\sigma} [T_{11}T_{22} - T_{12}T_{21}] V^{(i)} \ .
\end{aligned}$$

These expressions define the 4×4 matrix $\bar{F}$. Sometimes, the scattering of light is described with the set of parameters $\tilde{\mathbf{I}} = (I_l, I_r, U, V)$ instead of the Stokes parameter

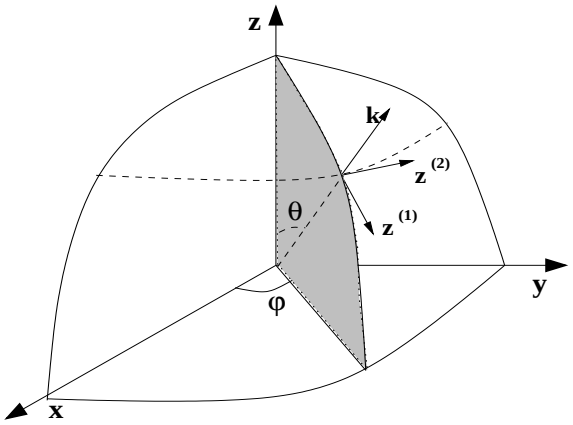

Fig. 7. Coordinate system for the Stokes vector. The shaded plane is the plane of reference, the meridian plane.

$\mathbf{I} = (I, Q, U, V)$. After the simple transformation $I = I_l + I_r$ and $Q = I_l - I_r$, the scattering matrix $\tilde{F}$ is:

$$\tilde{F} = \bar{\sigma} \begin{pmatrix} T_{11}^2 & T_{12}^2 & T_{11}T_{12} & 0 \\ T_{21}^2 & T_{22}^2 & T_{22}T_{21} & 0 \\ 2T_{11}T_{21} & 2T_{22}T_{12} & T_{11}T_{22} + T_{12}T_{21} & 0 \\ 0 & 0 & 0 & T_{11}T_{22} - T_{12}T_{21} \end{pmatrix}. \qquad (50)$$

References

1. J.S. Ryan and A.I. Carswell, "Laser beam broadening and depolarization in dense fog," *J. Opt. Soc. Am. A* **68**, 900–908 (1978).

2. L.R. Bissonnette, "Imaging through fog and rain," *Opt. Eng.* **31**, 1045–1052 (1992).

3. C. Werner, J. Streicher, H. Herrmann, and H.G. Dahn, "Multiple-scattering lidar experiments," *Opt. Eng.* **31**, 1731–1745 (1992).

4. R.F. Tusting and D.L. Davis, "Laser systems and structured illumination for quantitative undersea imaging," *Mar. Technol. Soc. J.* **26**, 5–12 (1992).

5. D.T. Delpy, M. Cope, P. Van der Zee, S. Arridge, S. Wray, and J. Wyatt, "Estimation of optical pathlength through tissue from direct time of flight measurement," *Phys. Med. Biol.* **33**, 1433–1442 (1988).

6. K.M. Yoo, B.B. Das, and R.R. Alfano, "Imaging of translucent object hidden in highly scattering medium from the early portion of the diffuse component of a transmitted ultrafast laser pulse," *Opt. Lett.* **17**, 958–960 (1992).

7. V. Sankaran, K. Schönenberger, J. T. Jr. Walsh, and Maitland D. J., "Polarization discrimination of coherently propagating light in turbid media," *Appl. Opt.* **38**(19), 4252–4261 (1999).

8. S. R. Arridge and J. C. Hebden, "Optical Imaging in Medicine: II. Modelling and reconstruction," *Phys. Med. Biol.* **42**, 841–853 (1997).

9. Przeslawski J. Michielsen K., DeRaedt H. and Garcia N, "Computer simulation of time-resolved optical imaging of objects hidden in turbid media," *Phys. Reports* **304**, 90–144 (1998).

10. O Dorn, "A transport-backtransport method for optical tomography," *Inverse Problems* **14**, 1107–1130 (1998).

11. S. L. Jacques, J. R Roman, and K Lee, "Imaging superficial tissues with polarized

light," *Laser. Surg. Med.* **26**(2), 119–129 (2000).

12. J. M. Schmitt, A. H. Gandjbakhche, and R. F. Bonner, "Use of polarized light to discriminate short-path photons in a multiply scattering medium," *Appl. Opt.* **31**, 6535–6546 (1992).

13. M.P. Rowe, E.N.Jr. Pungh, J.S. Tyo, and N. Engheta, "Polarization-difference imaging: a biologically inspired technique for observation through scattering media," *Opt. Lett.* **20**, 608–610 (1995).

14. S.G. Demos and R.R. Alfano, "Temporal gating in highly scattering media by the degree of optical polarization," *Opt. Lett.* **21**, 161–163 (1996).

15. J. M. Schmitt and G. Kumar, "Turbulent nature of refractive-index variations in biological tissue," *Opt. Lett.* **21**, 1310–1312 (1996).

16. F.C. Mackintosh and S. John, "Diffusing-wave spectroscopy and multiple-scattering of light in correlated random media," *Phys. Rev. B* **40**, 2383–2406 (1989).

17. F.C. Mackintosh, J.X. Zhu, D.J. Pine, and D.A. Weitz, "Polarization memory of multiply scattered-light," *Phys. Rev. B* **40**, 9342–9345 (1989).

18. D. Bicout, C. Brosseau, A.S. Martinez, and J.M. Schmitt, "Depolarization of multiply scattered waves by spherical d iffusers:Influence of the size parameter," *Phys. Rev. E* **49**, 1767–1770 (1994).

19. S. Chandrasekhar, *Radiative Transfer*, Oxford University Press, Cambridge, (1960).

20. L.E. Mertens and F.S. Replogle, Jr., "Use of point spread and beam spread functions for analysis of imaging systems in water," *J. Opt. Soc. Am. A* **67**, 1105–1117 (1977).

21. T. Aruga and T. Igarashi, "Narrow beam light transfer in small particles: image blurring and depolarization," *Appl. Opt.* **20**, 2698–2705 (1981).

22. Y. Kuga and A. Ishimaru, "Modulation transfer function and image transmission

through randomly distributed spherical particles," *J. Opt. Soc. A* **2**, 2330–2335 (1985).

23. L. Ryzhik, G. Papanicolaou, and J. B. Keller, "Transport equations for elastic and other waves in random media," *Wave Motion* **24**, 327–370 (1996).

24. A. Ishimaru, *Wave Propagation and Scattering in Random Media*, Academic Press, New York, (1978).

25. B. Beauvoit, T. Kitai, and B. Chance, "Contribution to the mitochondrial compartment to the optical properties of the rat liver: a theoretical and practical approach," *Biophys. J.* **67**, 2501–2510 (1994).

26. J.R. Mourant, J.P. Freyer, A.H. Hielscher, A.A. Eick, D. Shen, and T.M. Johnson, "Mechanisms of light scattering from biological cells relevant to noninvasive optical-tissue diagnostics," *Appl. Opt.* **37**, 3586–3593 (1998).

27. G.N. Plass and G.W. Kattawar, "Monte Carlo calculations of light scattering from clouds," *Appl. Opt.* **7**, 415 (1968).

28. Meier R.R., "Atmospheric scattering of middle uv radiation from an internal source," *Appl. Opt.* **17**, 3216–3225 (1978).

29. B. C. Wilson and G. Adam, "A monte carlo model for the absorption and flux distributions of light in tissue," *Med. Phys.* **10**, 824 (1983).

30. E. Tinet, S. Avrillier, and M. Tualle, "Fast semianalytical monte carlo simulation for time-resolved light propagation in turbid media," *J. Opt. Soc. Am. A* **13**, 1903–1915 (1996).

31. G. Zaccanti, "Monte Carlo study of light propagation in optically thick media: point source case," *Appl. Opt.* **30**, 2031–2041 (1991).

32. G.W. Kattawar and G.N. Plass, "Radiance and polarization of multiple scattered light from haze and clouds," *Appl. Opt.* **7**, 1519–1527 (1968).

33. P. Bruscaglioni, G. Zaccanti, and Q. Wei, "Transmission of a pulse polarized light beam through thick turbid media: numerical results," *Appl. Opt.* **32**, 6142–6150 (1993).

34. G. Bal, G. Papanicolaou, and L. Ryzhik, "Probabilistic Theory of Transport Processes with Polarization," *SIAM Appl. Math.* **60**, 1639–1666 (2000).

35. M. H. Kalos and P. A. Whitlock, *Monte Carlo Methods*, New York : J. Wiley Sons, (1986).

36. E. E. Lewis and W. F. Miller Jr., *Computational Methods of Neutron Transport*, John Wiley and sons, New York, (1984).

37. G. Bal and M. Moscoso, "Theoretical and Numerical Analysis of Polarization for Time Dependent Radiative Transfer Equations," *JQSRT* (in press).

38. G. Bal and M. Moscoso, "Polarization Effects of Seismic Waves on the Basis of Radiative Transport Theory," *Geophys. J. Int.* (in press).

39. M.H. Kalos, "On the estimation of flux at a point by Monte Carlo," *Nucl. Sci. Eng.* **16**, 111–117 (1963).

40. H.A. Steinberg and M.H. Kalos, "Bounded estimators for flux at a point in monte carlo," *Nucl. Sci. Eng.* **44**, 406–412 (1971).

41. H. Iida and Y. Seki, "Simple method of eliminating infinite variance in point detector problem of monte carlo calculation," *J. Nucl. Sci. Technol.* **17**, 315–317 (1980).

42. S. Chatigny, M. Morin, D. Asselin, Y. Painchaud, and P. Beaudry, "Hybrid monte carlo for photon transport through optically thick scattering media.," *Appl. Opt.* **38**, 6075–6086 (1999).

43. W.F. Cheong, *Summary of optical properties*, in Optical-Thermal Response of Laser-Irradiated Tissue, A.J. Welch and M.J.C. van Gemert eds. (Plenum, New York), (1985).

44. E.J. McCartney, *Optics of the Atmosphere*, John Wiley & Sons, (1976).

45. W.G. Egan, W.R. Johnson, and V.S. Whitehead, "Terrestrial polarization imagery obtained from the space-shuttle: characterization and interpretation," *Appl. Opt.* **30**, 435–442 (1991).